THE ASTROPHYSICAL JOURNAL, 400:562–578, 1992 December 1

INFRARED EMISSION FROM X-RAY AND OPTICALLY EMITTING REGIONS IN THE CYGNUS LOOP SUPERNOVA REMNANT

RICHARD G. ARENDT[1]
Applied Research Corporation, CDAC, Commerce Center II, Room 100, 7601 Ora Glen Drive, Greenbelt, MD 20770
ELI DWEK
Code 685, Laboratory for Astronomy and Solar Physics, NASA/Goddard Space Flight Center, Greenbelt, MD 20771
AND
DAVID LEISAWITZ
Astronomy Department, Pennsylvania State University, University Park, PA 16802
Received 1991 November 4; accepted 1992 June 10

ABSTRACT

We present a new technique for analyzing the infrared (IR) emission of a supernova remnant (SNR) and apply it to the Cygnus Loop. The technique consists of a decomposition of the IR emission from the remnant (in all four *IRAS* bands) into two distinct emission components. The first component is spatially correlated with the X-ray emission from the remnant and arises from collisionally heated dust in the shocked gas. The second component is spatially correlated with the optical filaments and arises from dust which is radiatively or collisionally heated within the filaments, and from IR lines emitted by the shocked gas. The decomposition allows us to determine the characteristics of the dust, examine evidence for grain processing through the shock, constrain various remnant parameters, and demonstrate how the morphology of the environment determines the IR emission from the remnant.

Subject headings: dust, extinction — infrared: interstellar: continuum — ISM: individual (Cygnus Loop) — supernova remnants

1. INTRODUCTION

The Cygnus Loop (G74.0 − 8.5) is a frequently studied supernova remnant (SNR), with a wealth of observational history. Minkowski (1958) derived the generally accepted distance of the Cygnus Loop (770 pc) from the radial velocities of the bright optical filaments, combined with the proper motions of the filaments reported earlier by Hubble (1937). The Cygnus Loop has also proved to be a strong source of synchrotron radio emission (e.g., Keen et al. 1973; Green 1990), IR emission (Braun & Strom 1986b), UV radiation (Blair et al. 1991), and X-rays (Ku et al. 1984). Detailed spectral studies in the optical and X-ray regimes have shown that there is a range of densities and shock velocities present in the Cygnus Loop. The slowest shocks in the denser clouds ($n \gtrsim 10$ cm^{-3}) give rise to the bright radiative optical filaments with strong forbidden line emission (Miller 1974; Fesen, Blair, & Kirshner 1982, hereafter FBK) and UV emission (Raymond et al. 1980a; D'Odorico et al. 1980). Faster shocks are adiabatic and characterized by weak Balmer emission (Raymond et al. 1980b; FBK; Hester, Raymond, & Danielson 1986), and UV emission (Raymond et al. 1983). Still faster shocks in the low-density ($n \sim 0.1$ cm^{-3}) intercloud ISM give rise to the hotter (few $\times 10^6$ K) X-ray emission which exhibits lines of highly ionized species (Vedder et al. 1986).

Most spectral regimes provide information on the gaseous component of the ISM as it is swept up and shocked by the SNR. The IR is unique in that only in the infrared do we obtain direct information on the solid (i.e., dust) component of the ISM. Additionally the IR can reveal morphology that is not visible at other wavelengths. Since many components of the ISM radiate in the IR, infrared observations can also reveal the relation between a SNR and its local environment. In this paper we examine the IR emission of the Cygnus Loop to learn about the heating and destruction of interstellar dust as it is swept up by the SNR, and to use the IR emission as a probe of the physical conditions within the Cygnus Loop.

In order to obtain any quantitative results from the IR data for the remnant, we need to remove as much of the unrelated line of sight emission (confusion) as possible. The best understood components of this confusing emission are the large-scale zodiacal and Galactic backgrounds. We removed the gradients of these backgrounds by subtracting models of the emission from the data (§ 2.1). The resulting IR maps were affected only by small-scale sources and the ubiquitous cirrus clouds.

To gain some physical insight to the processes giving rise to the IR emission within the Cygnus Loop, we compared the IR emission of the Cygnus Loop with the X-ray and optical emission. We expect correlations of emission in these wavelengths since a fraction of the IR emission is expected to arise from collisionally heated dust residing in the X-ray–emitting plasma with the remaining emission originating from cooler optically emitting filaments (Dwek 1988). From the morphological structure of the remnant at IR, X-ray, and optical wavelengths, we discovered that it is possible to decompose the IR emission of the Cygnus Loop into two components. One component is spatially associated with the X-ray emission, and the other is associated with the optical emission. These two components can account for virtually all of the IR emission from the Cygnus Loop. Through the separate analyses of the IR intensities and spectra of these two components we have identified the emission mechanisms producing the correlations, and we

[1] National Research Council/Resident Research Associate.

have used models of the emission to determine the physical properties of the gas and dust responsible for the IR emission.

In § 2 we describe the data which we used and the processing applied to remove the background emission. We remove components corresponding to the zodiacal and the smooth Galactic emission. The remaining faint structures in the images can be characterized as noise. Section 3 contains a description of how we constructed models of the IR emission from the X-ray and optical images. These models enable us to separate two distinct components of the IR emission. In § 4 we examine the component of the IR emission that is associated with the X-ray–emitting shell. This IR emission is found to be thermal continuum emission from collisionally heated dust grains. Section 5 contains an analysis of the component of the IR emission that is associated with the optical filaments. This emission is probably a combination of line emission and thermal emission from dust. The discussion in § 6 compares how the results of this work relate to those of previous studies of the Cygnus Loop. We also discuss the similarities and differences between the Cygnus Loop and other SNRs, and how these differences are related to the ages and environments of the SNRs. A final summary is given in § 7.

2. DATA AND PROCESSING

2.1. *Infrared*

The IR data are the primary focus of this research. These data were in the form of *IRAS* co-added images at 12, 25, 60, and 100 μm, created by the Infrared Processing and Analysis Center (IPAC). The co-added images are $8^\circ \times 8^\circ$ with 1′ square pixels. The orginal co-added images were not processed through the default flattening process normally employed by IPAC. This left clear gradients in the images due to zodiacal and Galactic emission. Rather than removing these gradients with arbitrary surfaces, we fitted backgrounds which had shapes based upon the expected geometries and spectra of each component. In other words, we subtracted a background, $I_B(\lambda)$, from each of the IR images of the form

$$I_B(\lambda) = I_{\rm Zodi}(\lambda) + I_{\rm Gal}(\lambda) + I_0(\lambda) . \quad (1)$$

By this process we aim to subtract "physical backgrounds" which are related to specific physically distinct dust components along the line of sight. While we do not intend to do any analysis of these background components, we are interested in removing all confusing emission arising from sources which we can identify, understand, and model.

In the following subsections we describe the removal of the zodiacal and Galactic background terms $I_{\rm Zodi}(\lambda)$ and $I_{\rm Gal}(\lambda)$, and the determination of the additional constant term (i.e., flat background) $I_0(\lambda)$.

2.1.1. *Zodiacal Emission*

The zodiacal emission, $I_{\rm Zodi}(\lambda)$, at high ecliptic latitudes, β, ($\beta = 46.^\circ1$ at the center of the Cygnus Loop) is reasonably modeled in the form (Hauser et al. 1984; Hauser & Vrtilek 1992)

$$I_{\rm Zodi}(\lambda) = A_Z(\lambda) \times \mathrm{cosec}\,(|\beta|) + C_Z(\lambda) . \quad (2)$$

We used a least-squares fitting procedure to find the best coefficient, $A_Z(\lambda)$, and constant, $C_Z(\lambda)$. To avoid forcing the fit through regions of emission from distinct small-scale sources, we excluded ("masked out") bright regions of the image. The masked regions were defined as those exceeding a specified intensity in images from which a rough estimate of the background had been removed (a second-order polynomial fit to all regions for the 25 μm image, and an estimated cosecant background for the 12 μm image).

This fit was performed on the 12 and 25 μm images independently with the results listed in Table 1. For the 60 μm image the zodiacal emission did not visibly dominate the large-scale emission, and thus could not be fitted by our method. Therefore we subtracted a scaled version of the 25 μm background from the 60 μm image. The scaling factor we used, $I_{\rm Zodi}(60\ \mu{\rm m})/I_{\rm Zodi}(25\ \mu{\rm m}) = 0.145$, corresponds to the observed colors of the zodiacal emission (derived from data presented by Hauser & Vrtilek 1992). We did not remove any 100 μm component of the zodiacal emission, since it has a negligible contribution to the background gradient. Hauser et al. (1984) estimate an intensity of 2–4 MJy sr^{-1} ($\sim 3 \times 10^{-8}$ W m^{-2} sr^{-1}) for the zodiacal emission at 100 μm at the ecliptic pole. At the latitude of the Cygnus Loop this will be $\sim 4.2 \times 10^{-8}$ W m^{-2} sr^{-1}, with variation of no more than 20% across the

TABLE 1

BACKGROUND EMISSION MODELS

PARAMETER	WAVELENGTH 12 μm	25 μm	60 μm	100 μm
$I_{\rm Zodi}$, zodiacal emission:				
Masking level (10^{-8} W m^{-2} sr^{-1})[a]	2.0	1.0	...	...
A_z (10^{-7} W m^{-2} sr^{-1})	8.34 ± 0.01	6.62 ± 0.01	0.960[b]	...
C_z (10^{-7} W m^{-2} sr^{-1})	8.483 ± 0.002	7.436 ± 0.001	1.078[b]	...
$I_{\rm Gal}$, Galactic emission:				
Masking level (10^{-8} W m^{-2} sr^{-1})[a]	...	...	1.5	2.5
A_G (10^{-6} W m^{-2} sr^{-1})	...	...	2.00 ± 0.03	2.84 ± 0.02
C_G (10^{-7} W m^{-2} sr^{-1})	...	...	0.409 ± 0.001[c]	1.369 ± 0.001
h_G (degrees)	...	...	1.758 ± 0.004	2.232 ± 0.003
θ_G (degrees)	...	...	144.60 ± 0.05	119.53 ± 0.03
I_0 (10^{-8} W m^{-2} sr^{-1})	−0.6	0.3	0.0	1.8
1 σ deviations (10^{-8} W m^{-2} sr^{-1})	2.3	1.2	1.8	2.3

[a] Any source which exceeded its local background level by an amount greater than the masking level was excluded by the background removal process.

[b] These values were not fitted but were selected as the product of the 25 μm fit and 0.145.

[c] This constant is dependent on the value of the constant term of the zodiacal fit.

entire image. While the total level of this background may be noticeable, its gradient across the image will be a fraction of the small-scale irregularities, and thus can be ignored. Therefore, the roughly constant level of the zodiacal emission at 100 μm has been absorbed into the constant term of the Galactic emission (below).

2.1.2. *Galactic Emission*

The gradient due to the Galactic emission was fitted in a process similar to that of fitting the zodiacal emission. We modeled the Galactic emission with an exponential function, which was not constrained to have a gradient normal to the Galactic plane

$$I_{\rm Gal}(\lambda) = A_G(\lambda) \times \exp\left(-\frac{b}{h_G(\lambda)}\right) + C_G(\lambda)\,, \qquad (3)$$

where

$$b = -x \sin\theta_G(\lambda) + y \cos\theta_G(\lambda)\,. \qquad (4)$$

The coordinates x and y are measured in degrees west and north, respectively, from the lower left corner of the images ($\alpha = 21^{\rm h}07^{\rm m}11^{\rm s}$, $\delta = 26°45'58''$). The parameter $h_G(\lambda)$ is the scale height of the gradient, and the parameter $\theta_G(\lambda)$ is the position angle (measured eastward from north in the usual equatorial coordinate system) of the gradient (both in degrees). We allowed all of the parameters to vary. The results from the best set of parameters are listed in Table 1.

We removed $I_{\rm Gal}(\lambda)$ from the 100 and 60 μm images. At 25 and 12 μm, the intensity of the Galactic emission, when modeled as a single-temperature blackbody based on the 60 and 100 μm data, is very low. Therefore, we did not remove any Galactic gradient from the 12 and 25 μm images. These images were already sufficiently flat across the region of the remnant after the zodiacal emission had been removed.

2.1.3. *Small-Scale Structure*

After the removal of the large gradients of the galactic and zodiacal emission as described above, we examined the resulting zero level of the maps in the immediate vicinity of the remnant. We found that the peak of the distribution of the pixel intensities was offset from the expected value of zero. (The region of emission from the SNR itself was excluded in this analysis.) We subtracted these offsets (I_0, the final term in eq. [1]) from the images to adjust the zero level locally in the region of the Cygnus Loop. These flat background components (Table 1) are only a fraction of the constant values which were removed from the images in the large-scale background fittings. The resultant zero levels are attained at similar locations outside the SNR in each of the bands. Maps of the final background subtracted images are shown in Figure 1. A color combination of the 12, 60, and 100 μm images is shown in Figure 2 (Plate 5). Note that the SNR can be distinguished from the surrounding cirrus emission by its higher color temperature.

It is because of the small-scale features (sizes $\lesssim 5'$) in the images that the background subtraction found a zero level which is appropriate for the whole image, but slightly in error for our particular region of interest. The emission of these small-scale structures cannot be removed and constitutes the greatest limitation to the accuracy of our measurements. The confusing structures can be characterized by the range of intensity variations across regions of each image in which no distinct bright sources are present. By treating the confusion as noise with an average value of zero across most regions, we define 1 σ variations in the data (which are listed in the last row of Table 1). These values will be used as if they represent the level of random noise remaining in the images.

2.2. *X-Ray*

For an X-ray image of the Cygnus Loop we used *Einstein* IPC images from Seward (1990). We combined the separate low and high pulse height images, but did so with a weighted sum so that the resulting image represented an integration over the energy band rather than the total number of photons. The IPC spectrum published by Ku et al. (1984) was used to determine that the low pulse height IPC image has an average of 0.3 keV per count, while the high pulse height IPC image has an average 1.2 keV per count. We multiplied each of the IPC images by these factors before adding the images together. A background level corresponding to 3.41×10^{-10} W m^{-2} sr^{-1} was then subtracted from the image so that a zero level was reached near the edge of the remnant. The total X-ray flux measured by Ku et al. (1984), $F_{\rm X} = 1.55 \times 10^{-11}$ W m^{-2}, was used to normalize the integrated emission from the remnant. The final image is shown in Figure 3.

2.3. *Optical*

The optical image we used is a narrow-band Hα + [N II] image (T. R. Gull, unpublished data). This image primarily shows the bright radiative shocks. Some of the faster adiabatic shocks are visible in the image particularly in the north-northeast, but they are rather faint. To achieve background levels similar to the other data, we first subtracted a second-order fit to the smooth background of the field. Next we identified the apparent locations of 25 SAO stars. The optical image was warped (using the IDL routine POLYWARP) with a third-order polynomial to make the optical locations of these stars coincide with the cataloged positions. The initial differences in position were 0–3 pixels. The image then was passed through a median-window filter with a width of 7 pixels (224″). This removed the stellar point sources, leaving the emission from the remnant relatively unchanged. A faint residual mottling with an average intensity of zero is present in the background. The image was finally transformed to the scale of the IR images and smoothed to a matching resolution. The intensity scale of the optical map is uncalibrated, but as with the X-ray data, it is the relative brightness which will concern us. The final image is shown in Figure 4.

3. DECOMPOSITION OF THE IR EMISSION INTO OPTICAL AND X-RAY COMPONENTS

3.1. *Definition of the XO Models*

The integrated IR emission of the remnant can be found by simply integrating the IR maps within the boundaries of the SNR. Using the 1.6×10^{-9} W m^{-2} sr^{-1} contour of the X-ray emission to define the outer boundary of the remnant, we find the integrated IR flux densities listed in Table 2. However, these values reflect the combined emission of very diverse regions of the remnant. Results more suitable for further analysis can be obtained if the flux densities of distinct emitting regions are measured separately.

To quantitatively examine the relation between the IR emission and the X-ray and optical emission we created empirical models in which the IR emission is given by a linear combination of the X-ray and optical emission from the remnant.

PLATE 5

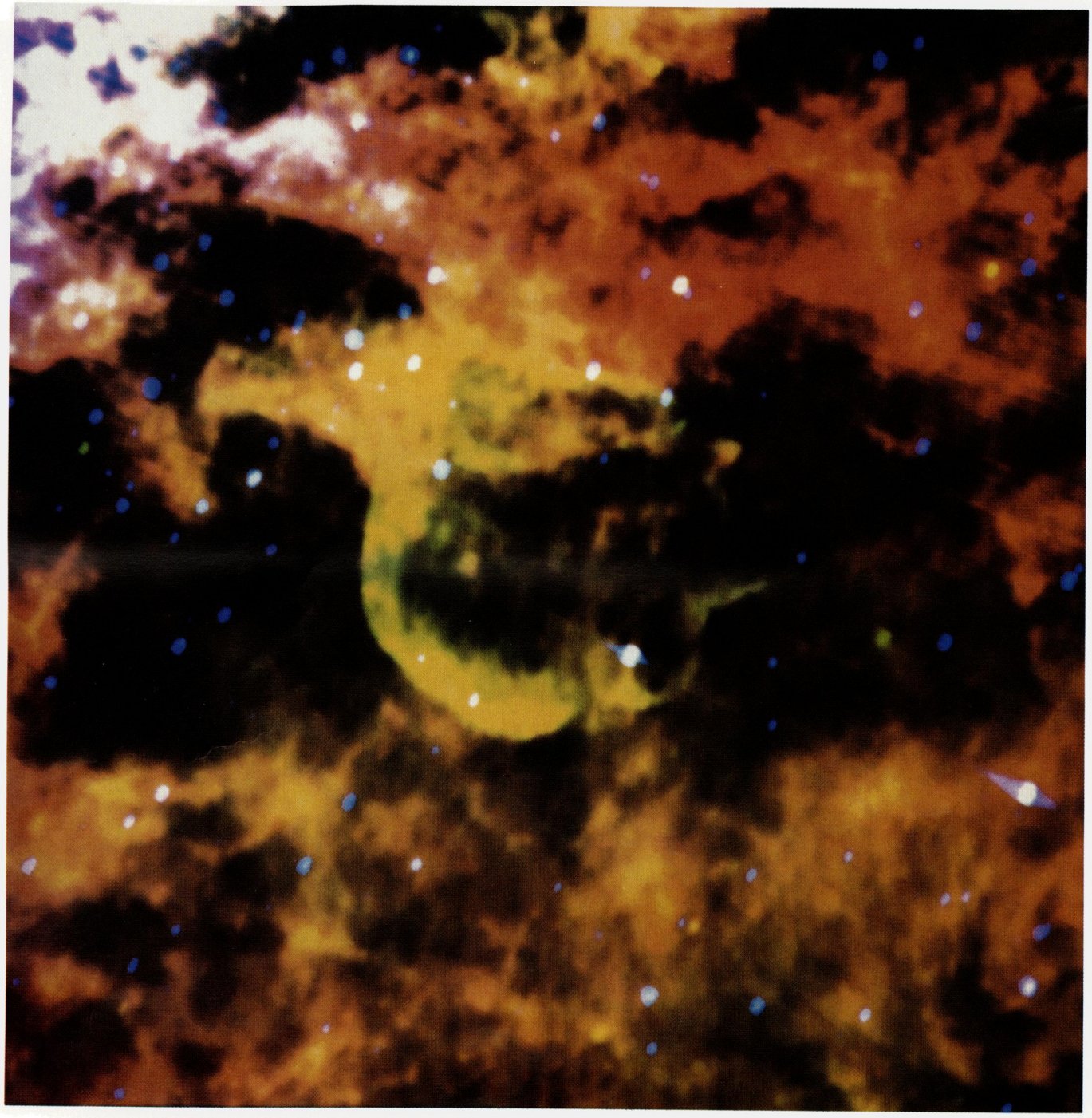

FIG. 2.—This color image of the Cygnus Loop shows 100, 60, and 12 μm emission as red, green, and blue respectively

ARENDT, DWEK, & LEISAWITZ (see 400, 564)

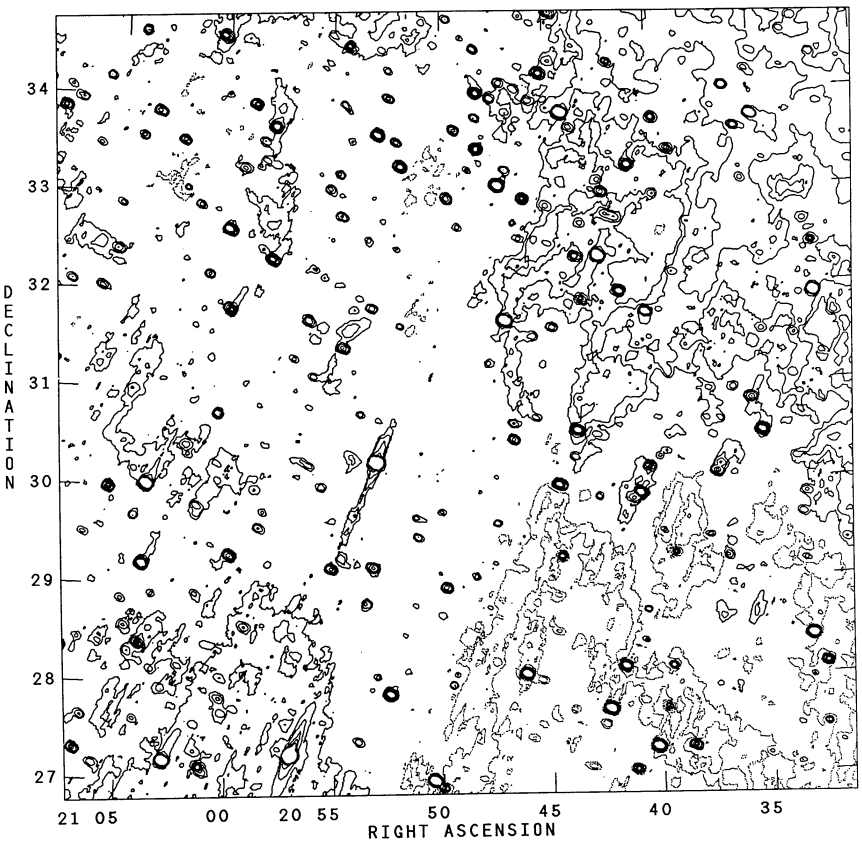

FIG. 1*a*

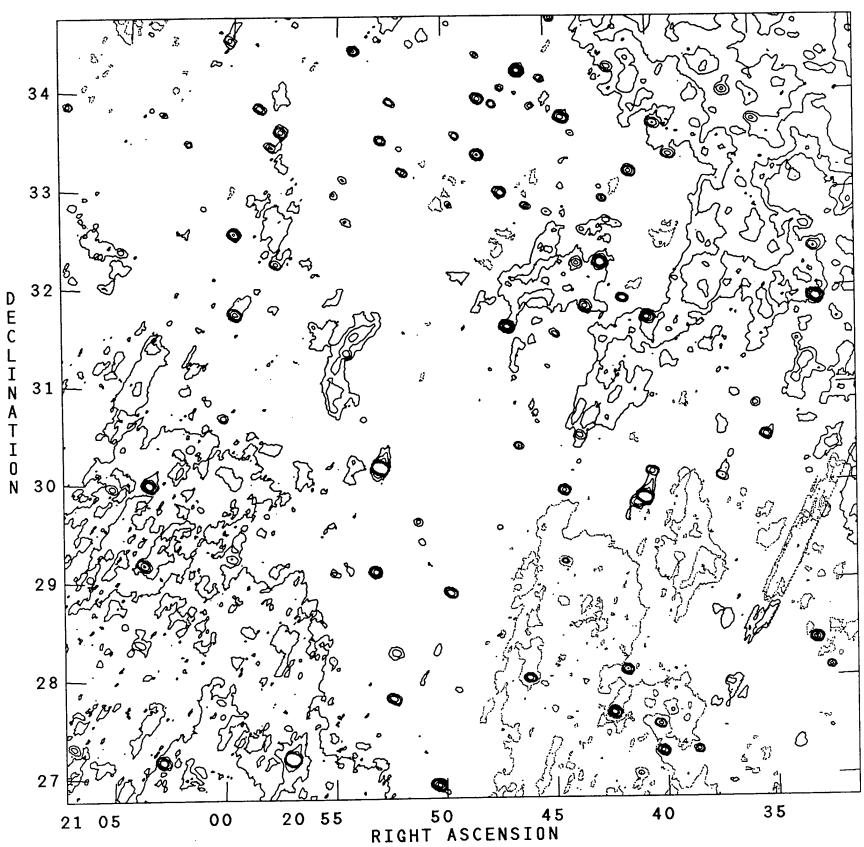

FIG. 1*b*

FIG. 1.—*IRAS* co-added maps of the Cygnus Loop and its environment after removal of background emission at (*a*) 12 μm, (*b*) 25 μm, (*c*) 60 μm, and (*d*) 100 μm

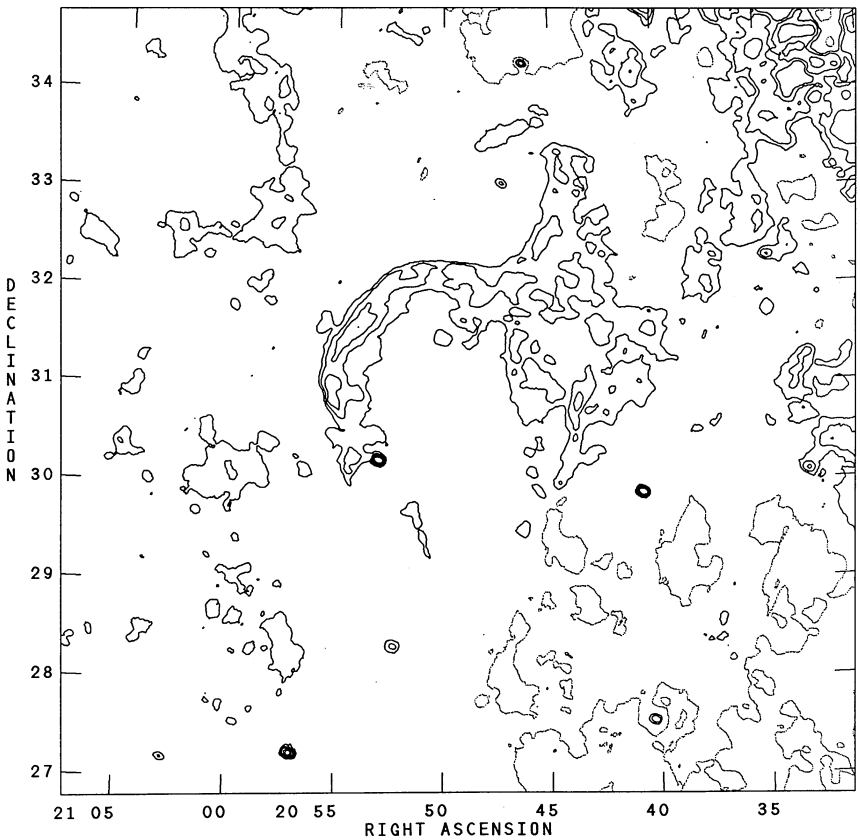

FIG. 1*c*

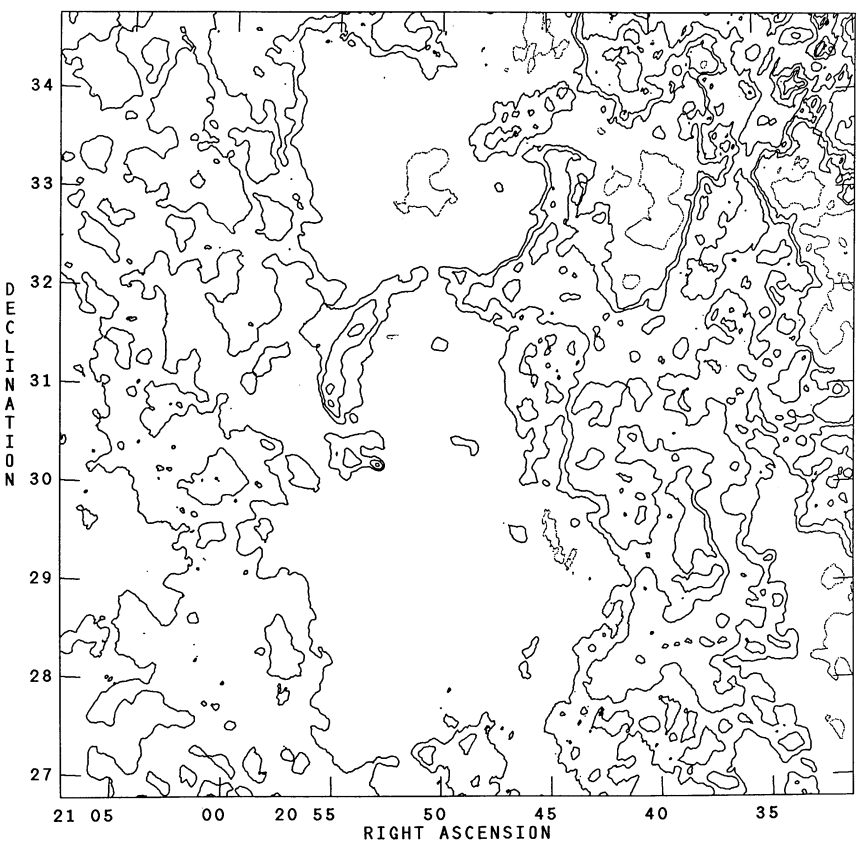

FIG. 1*d*

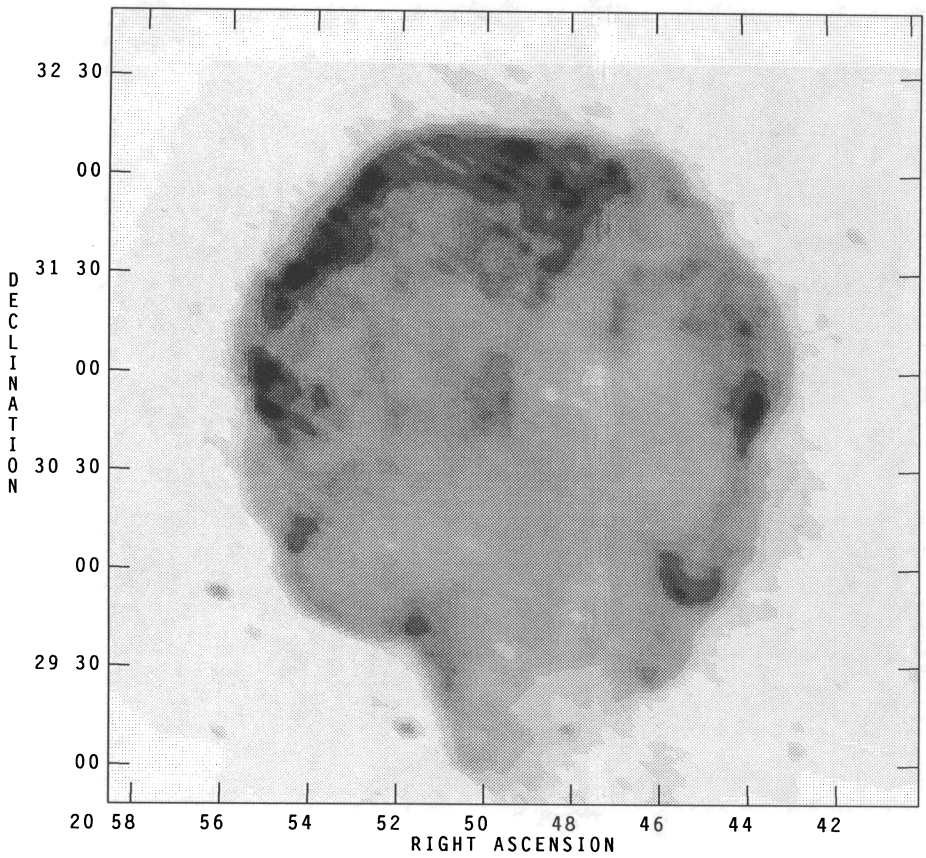

FIG. 3.—The *Einstein* IPC image of the Cygnus Loop (Seward 1990) after smoothing to the resolution of the *IRAS* data in Fig. 1

Ideally, these X-ray–optical (XO) models would fully account for the IR emission in each of the *IRAS* bands. We designate the IR intensity by $I_{IR}^{XO}(\lambda)$, where

$$I_{IR}^{XO}(\lambda) = I_{IR}^{X}(\lambda) + I_{IR}^{O}(\lambda) \quad (5a)$$

$$= A(\lambda)I_X + B(\lambda)I_O \, . \quad (5b)$$

The coefficients $A(\lambda)$ and $B(\lambda)$ are obtained by a least-squares fit, minimizing the difference between the model and the observed emission, $I_{IR}^{XO}(\lambda)$ and $I_{IR}^{Obs}(\lambda)$, on a pixel-by-pixel basis. In the event that either $A(\lambda)$ or $B(\lambda)$ was found to be negative, the negative coefficient was set to zero, and the fit was recalculated using only one component. It is important to point out that accurate determination of the coefficients $A(\lambda)$ and $B(\lambda)$ relies on the differences in morphology between the X-ray and the optical emission. If the X-ray and optical emission differed only by a scalar factor, it would be impossible to sort out their relative contributions. Fortunately, for the Cygnus Loop there are enough differences (even when limited by the resolution of the *IRAS* data) in the X-ray and optical emission for this procedure to work. Greater accuracy could be obtained if higher resolution data were used, where differences between the X-ray and optical emission are more distinct.

TABLE 2

IR FLUX DENSITY DECOMPOSITION INTO X-RAY AND OPTICAL EMISSION COMPONENTS

COMPONENT	WAVELENGTH			
	12 μm	25 μm	60 μm	100 μm
$I_{IR}^{X}(\lambda)$ (Jy)[a]	0	28	1650	2940
$I_{IR}^{O}(\lambda)$ (Jy)[a]	54	83	480	960
$I_{IR}^{X}(\lambda) + I_{IR}^{O}(\lambda)$ (Jy)[a]	54	111	2130	3900
$I_{IR}^{Obs}(\lambda)$ (Jy)[b]	48 ± 8	71 ± 11	2030 ± 30	4450 ± 110

[a] The uncertainties are estimated to be ~30% at 12 and 25 μm, and ~20% at 60 and 100 μm.

[b] The uncertainties reflect only the random errors due to residual background variations and not possible systematic errors in the background levels.

The coefficients $A(\lambda)$ and $B(\lambda)$ have physical significance. The coefficient $A(\lambda)$ is the ratio of IR to X-ray emission. This is the IRX ratio defined by Dwek et al. (1987b) with the modification that here the IR emission is measured only within a single *IRAS* band, i.e., $A(\lambda) = \mathrm{IRX}(\lambda)$. The total IRX ratio is $\mathrm{IRX} = 1.82 \times \sum \mathrm{IRX}(\lambda)$, where the factor of 1.82 accounts for IR flux which does not fall within any of the *IRAS* bands. For thermal X-ray emission and collisionally heated dust, the total IRX ratio is primarily a function of the gas temperature (Dwek et al. 1987b). The IRX ratio is a very simplified means of characterizing the complex interaction between dust (producing IR emission) and gas (producing X-ray emission) in a hot plasma. The $B(\lambda)$ coefficient has a similar interpretation, although the mechanisms relating the IR and optical emission are more complex (see § 5). In this analysis the $B(\lambda)$ coefficient can only be considered as a relative factor because we cannot determine the absolute calibration of the optical data.

In each IR band, XO models were calculated for a rectangular region covering the whole SNR, as well as over 12 independent subregions of the remnant (indicated in Fig. 5). The subregions were chosen to separate portions of the remnant which qualitatively have different morphologies or relative

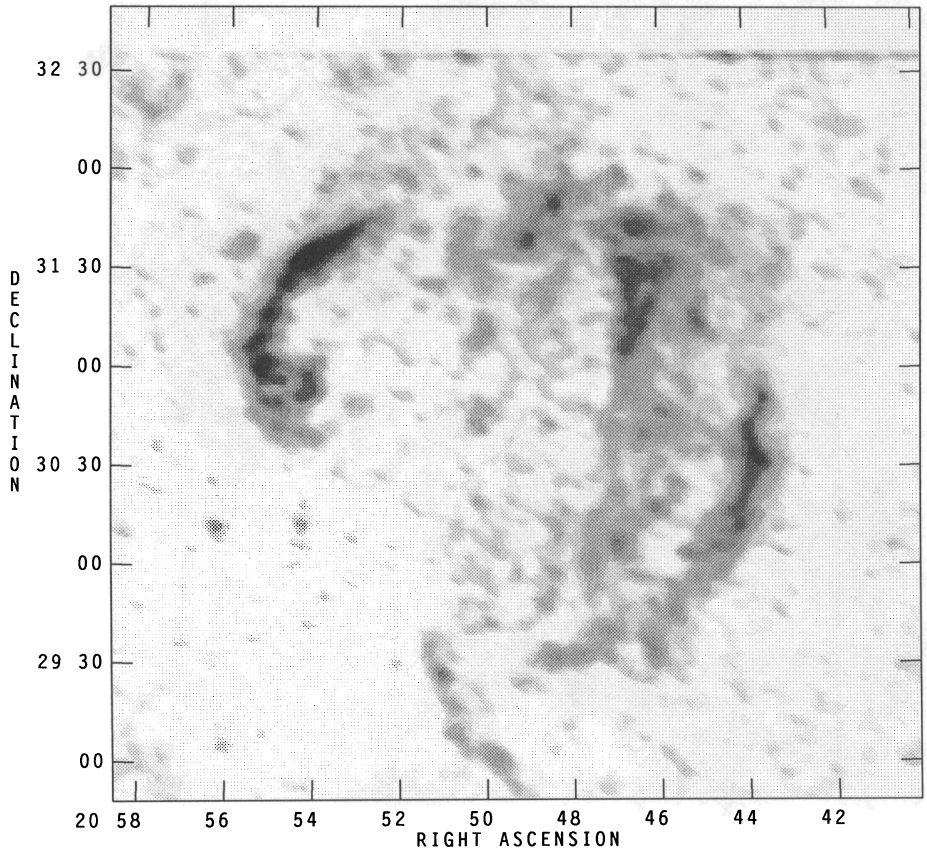

FIG. 4.—An optical Hα + [N II] image of the Cygnus Loop (T. R. Gull, unpublished data) after removal of stars and smoothing to the resolution of the *IRAS* data in Fig. 1.

X-ray and optical intensities. Most of the subregions are more nearly filled with emission from the SNR than is the region encompassing the entire Cygnus Loop. The XO models were calculated using IR images that had point sources and regions outside the SNR (as determined by its extent in the X-ray image where confusion is minimal) set to zero. This prevents artificial offsets in the fit due to confusing IR emission. The different regions chosen provide a global measure of the relationships between the IR and the X-ray and optical emission in addition to an assessment of local variations. The flux densities of the entire remnant for the best XO models in each band are listed in Table 2. In the absence of confusing emission or background errors, $I_{IR}^{XO}(\lambda)$ should be exactly equal to $I_{IR}^{Obs}(\lambda)$. Although the formal errors of the flux densities determined by the XO models are very small, visual inspection of the results indicates that variations of $A(\lambda)$ and $B(\lambda)$ by up to 20% can still produce acceptable models of the IR emission. The size of the uncertainties associated *only* with the measurement of the flux densities in the processed images (i.e., those due to the residual background level variations) are ~20% at 12 and 25 μm and ~2% at 60 and 100 μm. For the XO models we therefore adopt flux density uncertainties of 30% at 12 and 25 μm and 20% at 60 and 100 μm. Systematic errors in the background level could also introduce errors of this magnitude in the directly measured flux densities. We note that the total 100 μm flux density found by the direct integration of the IR images is likely to be overestimated. This is due to the presence of emission related to the complex features northwest of, and probably overlapping, the Cygnus Loop. The XO modeling should provide a better estimate of the flux density since it distinguishes the emission of the SNR from that of overlapping sources on the basis of morphology.

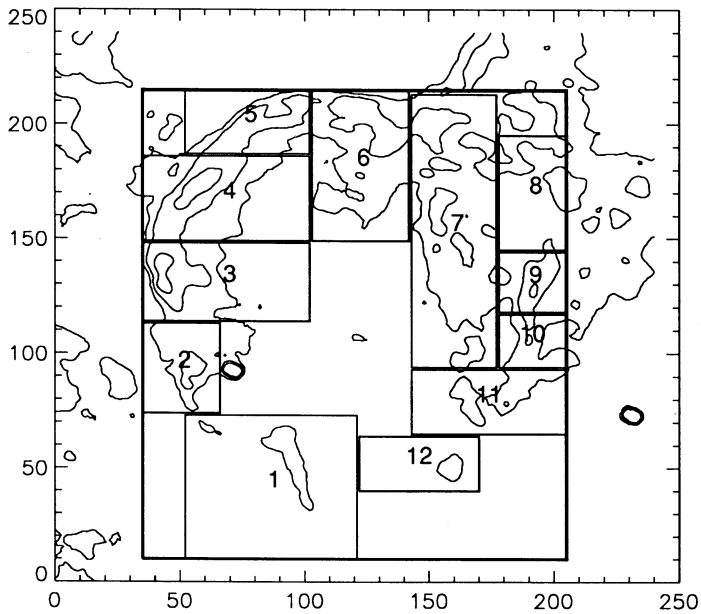

FIG. 5.—The areas used to fit the global (*heavy line*) and regional (*light lines*) XO models are indicated on this 60 μm contour map of the Cygnus Loop. The axes are labeled in arcminutes.

TABLE 3

XO MODEL COEFFICIENTS FOR THE CYGNUS LOOP[a]

	12 μm		25 μm		60 μm		100 μm	
REGION[b]	IRX(12)	$B(12)$[c]	IRX(25)	$B(25)$[c]	IRX(60)	$B(60)$[c]	IRX(100)	$B(100)$[c]
1	*0.068*	*0.00*	0.23	0.43	1.38	0.52	0.71	*0.00*
2	0.91	2.67	0.71	0.63	3.45	1.14	3.16	*0.32*
3	*0.00*	0.40	*0.00*	0.56	2.19	1.36	1.35	0.99
4	*0.00*	0.56	*0.0047*	0.53	2.79	1.10	1.46	0.83
5	*0.00*	*0.00*	0.055	0.35	2.95	1.66	1.38	1.60
6	*0.00*	0.25	0.035	0.14	2.32	0.33	1.63	0.20
7	2.25	0.44	0.57	0.17	3.83	0.78	5.44	0.28
8	0.43	*0.089*	*0.00*	0.42	3.04	3.41	3.17	2.40
9	0.91	0.38	0.25	0.70	2.98	0.88	3.97	*0.23*
10	*0.00*	0.075	*0.00*	0.17	0.40	1.02	*0.15*	1.34
11	*0.00*	*0.00*	*0.00*	*0.00*	1.24	0.41	0.87	0.50
12	*0.00*	*0.00*	*0.00*	0.063	0.60	0.63	1.34	0.30
Whole SNR	*0.00*	0.51	0.084	0.36	2.42	1.00	1.83	0.79

[a] Coefficients in italics are uncertain by >40%.
[b] Locations of the regions are indicated in Fig. 5.
[c] $B(\lambda)$ coefficients are normalized with respect to $B(60\ \mu m)$ for the whole SNR.

The $A(\lambda) = \mathrm{IRX}(\lambda)$ and $B(\lambda)$ coefficients of the X-ray and optical components for the whole SNR and the various subregions are presented in Table 3. Since the lack of calibration for the optical data makes only the relative values significant, the $B(\lambda)$ coefficients have been normalized to the 60 μm coefficient found for the remnant as a whole, which is the most accurate of the $B(\lambda)$ coefficients. Values of $A(\lambda)$ or $B(\lambda)$ which are uncertain by more than 40% are listed in italics. Most of the variations in $A(\lambda)$ and $B(\lambda)$ are because the X-ray and optical emission are too similar in morphology or too heavily confused within the small regions examined. The results presented in Table 3 should be taken as indicative only of the qualitative trends to be found around the remnant.

3.2. *Variations on the XO Models*

Variations on the XO modeling scheme were calculated by including a variable-intensity flat component as well as the X-ray and optical components

$$I_{\mathrm{IR}}^{\mathrm{XO}}(\lambda) = A(\lambda)I_{\mathrm{X}} + B(\lambda)I_{\mathrm{O}} + C(\lambda)\ . \qquad (6)$$

Other models used the *Einstein* HRI mosaics (Seward 1990) for the comparison X-ray data. These data suffer less from artifacts but cover only limited portions of the remnant. We also tried using an independently constructed IPC mosaic (courtesy R. Pisarski). None of these variations produced results significantly better than XO models using the IPC data presented above.

We also considered the possibility that a linear combination in the first order of the X-ray and optical emission (eq. [5]) may not be the most appropriate. The first-order linear combination contains the implicit assumption that the physical conditions are uniform throughout the remnant and all brightness variations (at all wavelengths) are due to differing line-of-sight thicknesses of optically thin emitting regions. As a check of this assumption we tried to assume the opposite picture, in which the line-of-sight thickness of the remnant is constant and all brightness variations are due to changes in temperature and/or density, and hence the emissivity. Assuming that the X-ray–associated IR emission is from collisionally heated dust, the work of Dwek (1986) indicates that the IR emissivity is proportional to $n^2T^{1.5}$, while the X-ray emissivity between 10^5 and 3×10^7 K varies roughly as $n^2T^{-0.5}$ (e.g., Raymond, Cox, & Smith 1976). Therefore we see that if we assume that the remnant is isothermal, then the ratio of IR to X-ray emissivities will be constant and linear XO models apply. However, a more appropriate assumption may be that the remnant is isobaric (nT is constant) In this case the IR emissivity will scale as $n^{0.5}$, while the X-ray emissivity will scale as $n^{2.5}$. Thus for an isobaric SNR the IR emissivity will scale as the $\frac{1}{5}$ power of the X-ray emissivity. Models using a linear combination of X-ray emission to the $\frac{1}{5}$ and optical emission,

$$I_{\mathrm{IR}}^{\mathrm{XO}}(\lambda) = A(\lambda)(I_{\mathrm{X}})^{1/5} + B(\lambda)I_{\mathrm{O}}\ , \qquad (7)$$

fit poorly compared to the first-order versions (eq. [5]). While the true situation is probably somewhere between these extremes, it seems that most of the brightness variations are due to differing column lengths rather than differing physical conditions and emissivities. Therefore, we have used the first-order models, keeping in mind that there may be some locations where emissivities are noticeably different from the average.

3.3. *Success of the XO Models*

The effectiveness of the XO model can be seen in correlation plots of IR versus X-ray intensity and IR versus optical intensity, and in the residuals left after the XO model is subtracted from the IR data. Fairly good pixel-to-pixel correlation is seen between the IR and X-ray images (Fig. 6*a*). There is also a significant optical-IR correlation (Fig. 6*b*), but it is not as tight as that with the X-rays. However, the best correlation is found between the IR and the linear combination of the X-ray and optical emission indicated by our model (Fig. 6*c*). This is strong evidence that at least two components are present in the IR emission of the Cygnus Loop. The sharp boundary on the upper left of the distribution in Figure 6*c* indicates that there is relatively little optical and X-ray emission from confusing sources. The larger scatter toward higher IR intensities presumably reflects the emission of IR sources unassociated with the remnant. Other than indicating the quality of the two-component model, however, this plot provides little insight to the mechanisms at work in the remnant, since it depicts the total emission from both X-ray and optically emitting regions, which are only loosely correlated across the remnant.

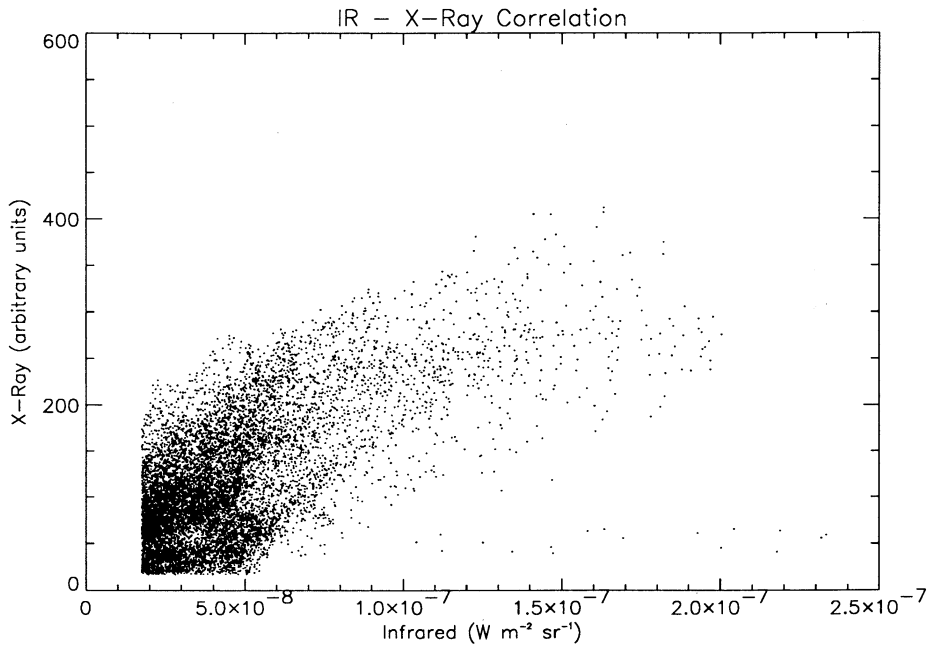

FIG. 6*a*

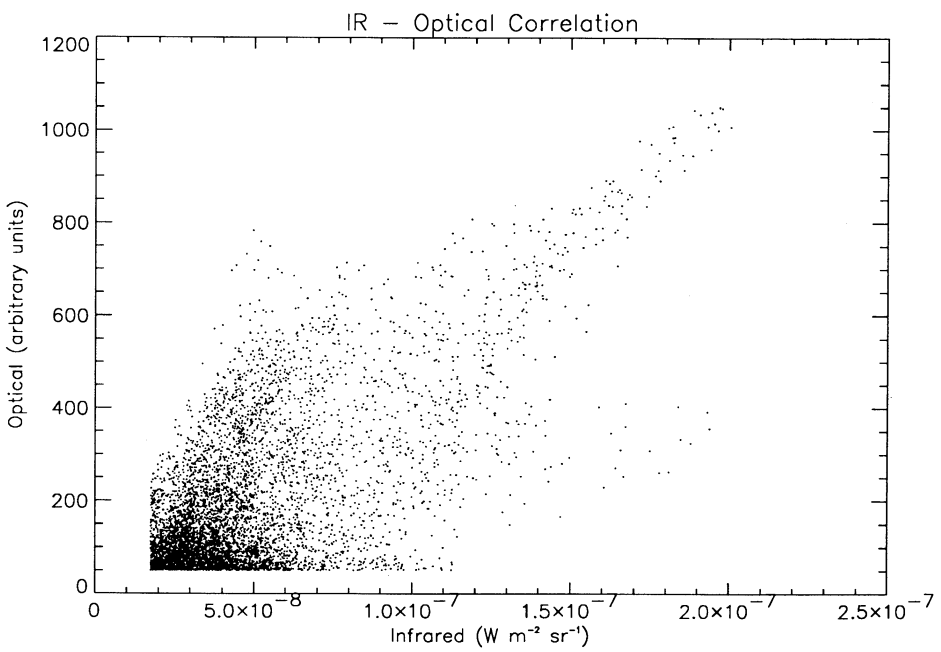

FIG. 6*b*

FIG. 6.—Correlations of pixel intensities between (*a*) 60 μm and X-ray data, (*b*) 60 μm and optical data, and (*c*) 60 μm data and best global XO model

The XO models are most effective at 60 μm, as evidenced in the residual map, due to the high relative brightness of the remnant compared to the confusing emission in this band. Figure 7 shows the 60 μm emission of the Cygnus Loop before and after the subtraction of our model. The residuals are generally at the level of the background variations. Some of the residuals associated with the SNR can be traced to artifacts in the IPC X-ray mosaic image; others may be caused by errors in the local background level. At some locations, however, the residuals probably reflect real variations in the relationship between the IR and the X-ray and optical emission. The one likely spot for such variation is at $\alpha = 20^{h}55^{m}.3$, $\delta = 30°50'$. This location appears as a knot of very soft X-ray emission (Ballet & Rothenflug 1989). It also coincides with a region believed to be the site of very recent interaction between the SNR and an interstellar cloud (Hester & Cox 1986). However, these correlations do not explain why this region should be the only location within the remnant with such an excess of IR emission. Also visible in the residual map (particularly in the W and NW) is IR emission from extended H I and CO clouds

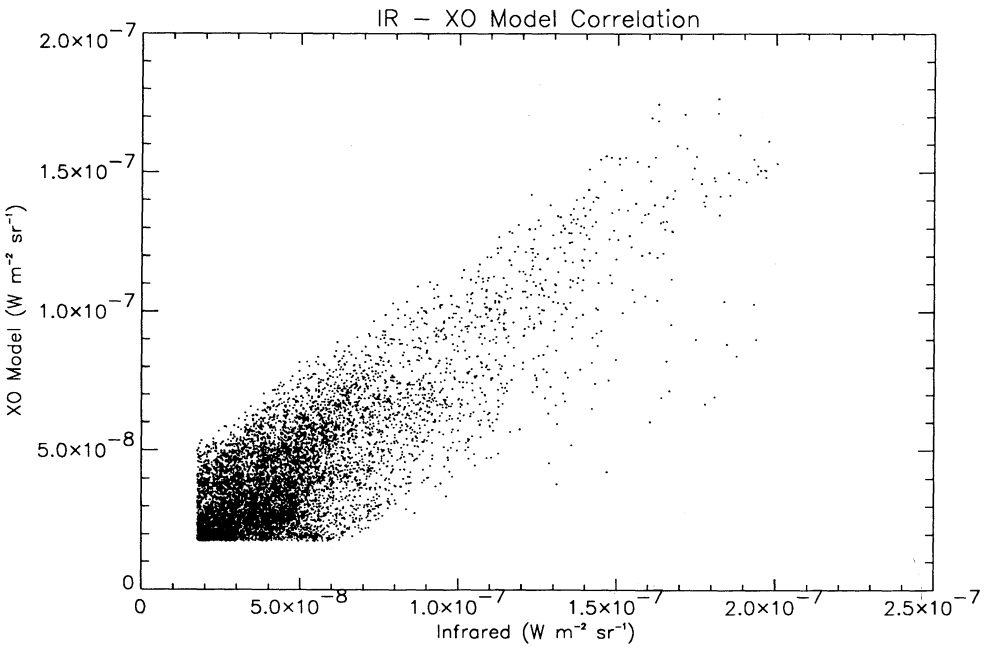

FIG. 6c

mapped by DeNoyer (1975), and Scoville et al. (1977). The extent of this IR emission across the western half of the SNR is very similar to that of fainter diffuse optical and radio emission (see Fig. 1 of Green 1990).

The success of the decomposition depends on the differences between the optical and X-ray morphologies of the remnant. A visual inspection of the images identifies differences which are large enough for this decomposition process. To test the robustness of our decomposition algorithm, in a more quantitative way, we constructed composite maps consisting of X-ray and optical emission added in different proportions. These artificial maps where then processed the same way as the real IR data, in order to examine to what accuracy we could retrieve the (known) ratio of components. In the absence of noise, our methods can accurately extract the X-ray and optical components even when one component dominates the other by factors of 10^2 or more. Adding an additional random noise component does not affect the derived X-ray or optical coefficients by more than a few percent unless the noise reaches levels comparable to one of the signals. The algorithm does somewhat worse when an offset is added to a linear combination of the X-ray and optical emission. However, our background subtraction efforts (§ 2) should keep this from being a serious problem.

The numerical tests of our decomposition algorithm convinced us of the reliability of the temperatures we derive for each emission component. The fact that the variations in the 60–100 μm flux ratio around the remnant are not correlated with the relative intensities of X-ray and optical emission, explains why the derived color temperature for each component is similar. The equilibrium temperature of large grains depends only on the rate of energy deposition in the dust, irrespective of the form of the incident energy (photons, or particles). Therefore, if IR line emission can be ignored, the similarity in the 60–100 μm color temperature between the optical filaments and the X-ray shell (Table 4) reflects a similar energy deposition rate in the dust. For given plasma conditions, one can construct a variety of models for the radiation field that can meet this constraint. The presence of significant line emission will add an additional degree of freedom in constructing models for the radiation field. In any case, the similarity of the 60–100 μm color temperatures which we have derived for the X-ray and optical components of the IR emission is difficult to explain in detail, given the low spectral and spatial resolution of the present IR data. If data with arcsecond resolution were available, we might expect to see a rich variety of relations between IR and optical or X-ray emission, but perhaps no perfect correlations. Such is the case in comparing the X-ray and optical emission (e.g., Hester & Cox 1986) or in comparing near-IR H_2 emission with the optical filaments (Graham et al. 1991).

4. THE IR COMPONENT ASSOCIATED WITH THE X-RAY SHELL

Now that we have developed a means of separating the IR emission of the X-ray–emitting shell from that of the optical filaments, we can properly compare the IR and X-ray fluxes both globally and locally. In this section we first derive some average properties of the gas and dust which comprise the X-ray–emitting shell. Additional discussion concerning the methods for deriving these global properties is found in Dwek

TABLE 4

DUST AND GAS MASSES ASSOCIATED WITH X-RAY–EMITTING SHELL AND OPTICAL FILAMENTS

Component	$T_{60-100\mu m}$ (K)	$M_{dust}(M_\odot)$[a]	$M_{gas}(M_\odot)$[a]
Total SNR[b]	29	1.1	150
X-ray shell[c]	31	0.5	70
Optical filaments[c]	30	(0.20)	(27)

[a] Uncertainties are ~50%.
[b] Directly from IR data.
[c] Derived from XO model.

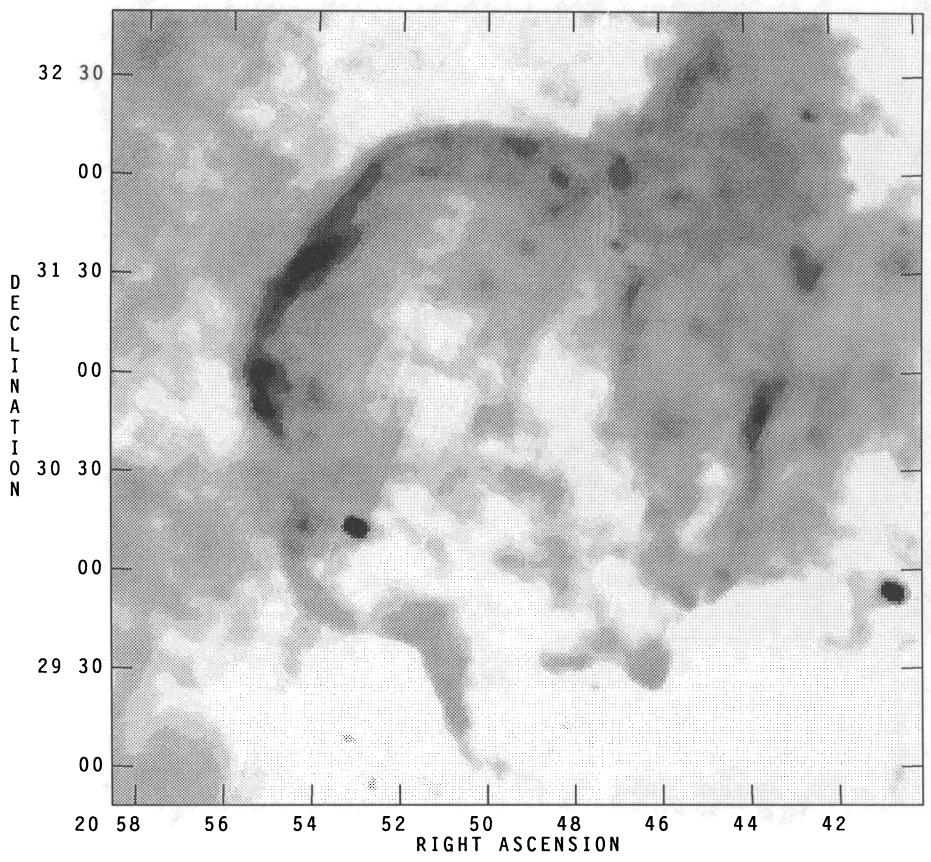

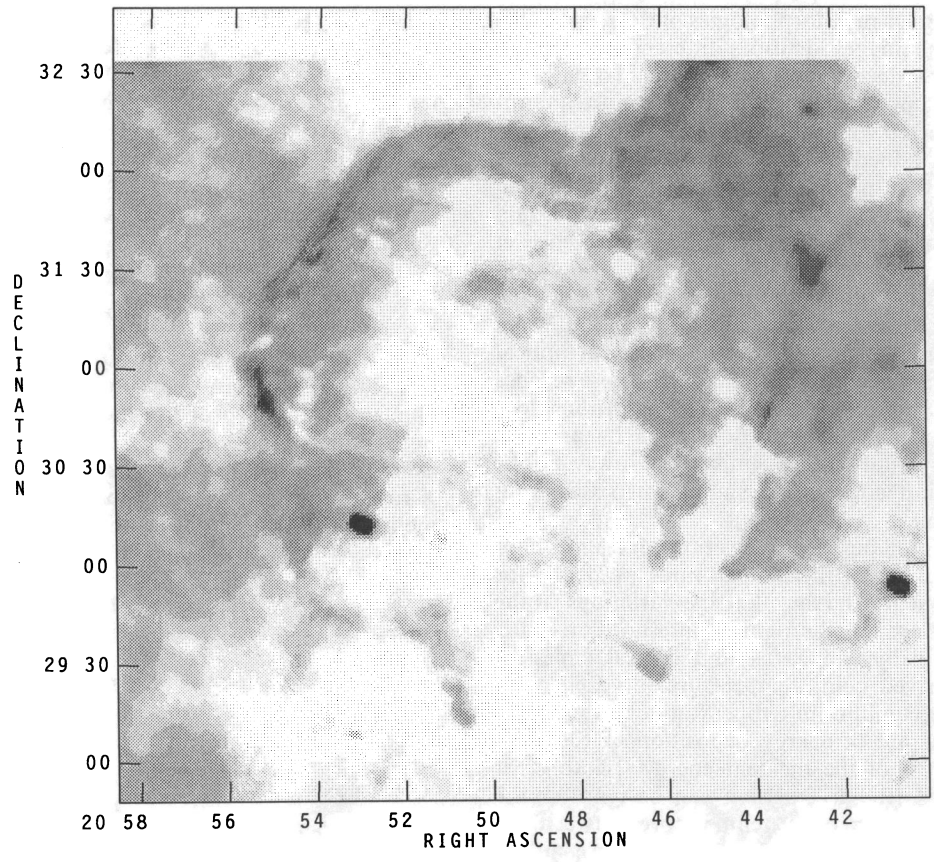

FIG. 7b

FIG. 7.—(*a*) The Cygnus Loop at 60 μm. (*b*) The residuals which remain at 60 μm after the XO model is subtracted from the *IRAS* data. The gray-scale levels are identical in both halves of this figure. Note that the residual emission from the remnant is generally at the level of the surrounding confusing emission.

& Arendt (1992). Then we apply a more detailed model of the IR emission (Dwek 1986) to examine how the grain sizes, and gas temperature and density, are constrained by the IR and X-ray observations. We use this model for the integrated emission of the X-ray shell, as well as for the emission of specific small portions of the shell which have been studied in detail in the X-ray regime.

4.1. *Global Analysis of the IR and X-Ray Shell*

A basic physical property of the remnant is the mass of the gas and dust which it has swept up. Initially we will assume that the IR emission mechanism is thermal radiation from dust grains. The mass of dust ($M_{\rm dust}$) in the SNR can be calculated from the IR observations by applying

$$M_{\rm dust} = 4\pi d^2 S_\lambda / \kappa_\lambda B_\lambda(T_{\rm dust}) \quad (8)$$

where d is the distance to the remnant, S_λ is the IR flux density, κ_λ is the mass absorption coefficient (we find $\kappa_{60} \approx 114$ cm^2 g^{-1}, $\kappa_{100} \approx 39.9$ cm^2 g^{-1} for dust which is $\sim$40% graphite and 60% silicate by mass using optical constants from Draine & Lee 1984), and $B_\lambda(T_{\rm dust})$ is the Planck function evaluated at the dust temperature. The dust temperature is approximated by the 60–100 μm color temperature of 31 K. However, a fraction of the 60 μm flux is provided by stochastically heated dust radiating at higher than equilibrium temperature; thus the dust temperature may be overestimated and the mass may be underestimated. The dust mass derived using equation (8) is $\sim 0.5\ M_\odot$ (Table 4). Division of the dust mass by a typical dust-to-gas mass ratio of 0.0075 gives the gas mass of $\sim 70\ M_\odot$ with the assumption that there has been no grain destruction. If significant grain destruction has occurred, then the gas mass will be higher than this estimate. The derived masses of gas and dust depend on the assumed distance of the Cygnus Loop. If the distance to the Cygnus Loop is 460 pc (Braun & Strom 1986b) rather than 770 pc (Minkowski 1958), then the masses quoted in Table 4 are too high by a factor of ~ 3. For comparison, the masses of dust and gas derived from the total IR emission measured directly from the co-added *IRAS* data are also listed in Table 4.

From the mass of the IR and X-ray–emitting shell ($70 \pm 35\ M_\odot$), and the radius (~ 18 pc not counting the breakout in the south, at 770 pc distance), we find the initial mean density of the ISM which has been swept up to form the X-ray shell is $n_0 = 0.074 \pm 0.037$ cm^{-3}. The dust temperature (31 K) is a function of the gas density ($n_{\rm gas} = 4n_0$) and temperature, so from the dust temperature and gas density we derive (Dwek 1987) $T_{\rm gas} = 3.3 \pm 2 \times 10^6$ K. If the shell is adequately described by the Sedov solution (e.g., Dwek 1981), we estimate an age of 15,000 $\pm$ 4000 yr and an initial explosion energy of $E_0 = 2.6 \pm 0.2 \times 10^{50}$ ergs. The energy estimate is in the same range as estimates from the X-ray emission (3×10^{50} ergs, Ku et al. 1984) and Braun & Strom's (1986b) IR analysis ($1.8–7.5 \times 10^{50}$ ergs, depending on the geometry of the surrounding medium).

We can gain additional information on the physical conditions within the SNR and on the size distribution of the radiating dust through the use of models containing more details concerning the size distribution and the heating of the dust grains (Dwek 1986, 1987). These detailed models are characterized by a size distribution of grains which is a power law in size ($\sim a^{-k}$) extending from $a_{\rm min}$ to $a_{\rm max}$, for both graphite and astronomical silicates. This form of the size distribution of grains was suggested by Mathis, Rumpl, & Nordsieck (1977) to explain interstellar optical and UV extinction, and will be referred to as an MRN size distribution. The gas temperature and density are used to calculate the collisional heating of a given size distribution of graphite and silicate dust grains. The stochastic nature of the heating is an essential part of the model. The resulting spectrum from small grains, for which the effects of stochastic heating are prominent, and large grains, which radiate at equilibrium temperatures, is compared to the observed spectrum, with the normalization factor determining the total mass of dust required. We adjust the input parameters of the model within constraints to find the optimum values for a match between the model and observed spectra. These models of the IR emission from collisionally heated dust have been previously applied to the remnants Cas A (Dwek et al. 1987a) and Puppis A (Arendt, Dwek, & Petre 1991).

The collisional heating model was applied to the IR emission associated with the X-ray shell. We limited our investigation of the density–temperature parameter space to the range of densities and temperatures which were found appropriate from X-ray studies of specific regions of the SNR (Ku et al. 1984; Charles, Kahn, & McKee 1985; Ballet & Rothenflug 1989). We adjusted the grain size distribution as a free parameter in order to find models which best matched the observations. The slope of the power law was kept fixed at $k = 3.5$, and the maximum grain size was fixed at $a_{\rm max} = 0.25$ μm (Mathis et al. 1977). The minimum grain size $a_{\rm min}$ and the amount of grain destruction by sputtering were varied.

As suggested by the lack of detected 12 μm emission and low 25 μm emission (Table 2), we find that small grains are underabundant compared to the general ISM and other dusty IR sources (e.g., Draine & Anderson 1985; Weiland et al. 1986). If this deficit of small grains is represented as a cutoff on the small end of the grain size distribution (with no grain destruction) then the minimum size of both graphite and silicate grains is in the range of $a_{\rm min} \approx 100$ Å (for $n = 0.1$ cm^{-3}, $T = 2.5 \times 10^6$ K) to $a_{\rm min} \approx 300$ Å (for $n = 0.56$ cm^{-3}, $T = 2 \times 10^6$ K). The optimum $a_{\rm min}$ increases with density. The best fit is achieved

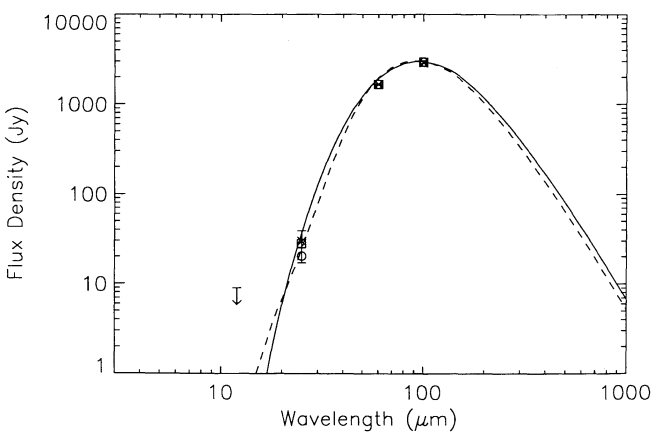

FIG. 8.—IR emission of the X-ray shell is indicated by the boxes with error bars. The solid line indicates the emission of a MRN distribution of grains with a minimum size $a_{\rm min} = 140$ Å collisionally heated by a plasma at $n = 0.18$ cm^{-3}, $T = 2.5 \times 10^6$ K, and the crosses show that emission integrated within the *IRAS* bands. The dashed line and open circles show the same quantities for an MRN distribution of grains subjected to sputtering of $\Delta a_{\rm sput} = 290$ Å and heated in a plasma of $n = 0.56$ cm^{-3}, $T = 2 \times 10^6$ K. These are the best models of the observed IR emission.

with $a_{min} \approx 140$ Å (for $n = 0.18$ cm^{-3}, $T = 2.5 \times 10^6$ K). This model is illustrated in Figure 8. We also considered reduction of the abundance of small grains through thermal sputtering. The effect of thermal sputtering is to reduce the size of all grains (irrespective of their initial sizes) by the same amount Δa_{sput}. The value of Δa_{sput} is related to the gas temperature and density and the residence time τ_{sput} in the hot gas by Δa_{sput} (μm) $= 10^{-6} n_{gas}$(cm^{-3})τ_{sput}(yr) for $T_{gas} \gtrsim 10^6$ K (Draine & Salpeter 1979; Seab 1987). When sputtering is invoked the best fit is achieved with $\Delta a_{sput} \approx 290$ Å ($a_{min} = 3$ Å, $a_{max} = 0.25$ μm, $k = 3.5$) for $n = 0.56$ cm^{-3}, $T = 2 \times 10^6$ K (also shown in Fig. 8). This amount of sputtering implies that the dust has been immersed in the hot gas for $\tau_{sput} \sim 1.2 \times 10^5$ yr, which is greater than the age of the remnant (~ 1–2×10^4 yr). All other reasonable models indicate that $\tau_{sput} \gtrsim 8 \times 10^4$ yr. (Note that as long as the initial a_{min} of the grain size distribution is less than Δa_{sput}, the fit is independent of a_{min} since all grains with sizes less than Δa_{sput} are destroyed. However, the initial value of a_{min} is important in calculating the fraction of dust which has been destroyed.) The fact that the sputtering time scale is longer than the age of the remnant indicates that either the IR emission is not thermal emission from a distribution of sputtered dust grains, or the small grains have already been depleted before the dust is swept up by the SNR. If small grains were present in normal abundances in the diffuse ISM surrounding the Cygnus Loop, we would expect detectable levels of 12 μm emission correlated with the X-ray emission.

By either method of representing the deficiency of small grains in the models above, the mass of dust required to produce the IR emission is $\gtrsim 0.75\ M_\odot$, and thus the mass of gas associated with the dust is $\gtrsim 100\ M_\odot$, assuming a dust-to-gas mass ratio of 0.0075. This is a factor of 2–3 higher than was found by the parameterized analysis used at the beginning of this section.

4.2. *Regional Analysis of the IR and X-Ray Shell*

More precise measurements of remnant properties can be made by examination of homogeneous subregions of the remnant. Thus, we also have modeled the IR emission observed for small regions whose X-ray spectral properties have been studied (Charles, Kahn, & McKee 1985, hereafter CKM; Vedder et al. 1986; and Ballet & Rothenflug 1989). The X-ray studies provide the gas temperatures necessary for application of the detailed dust emission model described in § 4.1. The significant result to note from these models is that for small regions of the remnant, as for the whole SNR, a distinct deficiency of small dust grains is indicated. Taking this as a sign of sputtering, the cooler, denser regions (the Ballet & Rothenflug 1989 regions) are best fitted by $\Delta a_{sput} \approx 640$ Å. Such amounts of sputtering are achieved in 4–8×10^4 yr. The other regions examined require comparable amounts of sputtering, implying time scales $> 2 \times 10^5$ yr. As found for the X-ray shell as a whole, these time scales are several times greater than the estimated age of the SNR. Combined with the similar sputtering derived for environments of different densities, these time scales suggest that the lack of small grains is an initial condition. It appears that the diffuse medium surrounding the Cygnus Loop is deficient in small dust grains. This conclusion applies only to the diffuse component of the medium through which the fast X-ray–producing shocks travel. A denser component of the medium is responsible for the slower shocks which produce the optically observed filaments.

4.3. *IRX Ratio Variations*

Variations in the IRX ratio can be used to determine if there are significant differences in physical conditions or the mechanism connecting the IR and X-ray emission around the remnant. Comparison of various slices through the IR and X-ray data indicate that the IRX ratio is up to a factor of 2 lower at the interior of the remnant than at the edges. This is contrary to what we had expected. Hotter plasma found in the interior portions of the shell (CKM; Tsunemi et al. 1988; and Hatsukade & Tsunemi 1990) should exhibit a higher IRX ratio, independent of density (Dwek et al. 1987b). The fact that we see no increase or even a decrease of the IRX ratio towards the center of the remnant could indicate that (1) the true IR background level has a minimum at the center of the SNR and rises toward the edges, and thus our background subtraction has systematically underestimated the IR emission in the central portions of the remnant, and/or (2) a large fraction of the dust in the interior of the remnant has been destroyed. There are no significant changes in the IRX ratios around the circumference of the SNR, as indicated by the 12 subregions (Table 3). This means that gas and dust characteristics of the shell are relatively uniform at a resolution of $\gtrsim 1'$, or that they conspire to vary in such a way as to keep the IRX ratio fairly constant.

5. THE IR COMPONENT ASSOCIATED WITH THE OPTICAL FILAMENTS

The analysis of the IR emission associated with the optical filaments is more difficult than that of the emission associated with the X-ray shell because the optical filaments have higher densities, lower temperatures, and a strong UV and optical radiation field. In such an environment we must consider collisional and radiative heating of dust, and line emission as possible contributors to the IR emission, as opposed to the X-ray shell where collisional heating is the dominant mechanism.

5.1. *Thermal Emission from Dust in the Optical Filaments*

First we proceed under the assumption that the IR emission of the optical filaments is thermal emission from dust embedded in the filaments. The 60–100 μm color temperature and mass of dust in the filaments were derived in the same manner as the mass of the X-ray shell (§ 4.1). We find $\sim 0.2\ M_\odot$ of dust and $\sim 26\ M_\odot$ of gas associated with the filaments (Table 4).

To examine the possibility that the dust is collisionally heated, we need to know the gas temperature and density in the filaments. Analysis of optical spectra from various locations around the Cygnus Loop indicate that typical temperatures are $\sim 2 \times 10^4$ K, and typical densities are ~ 100 cm^{-3} (FBK). From the work of Dwek (1987) we can calculate the equilibrium temperatures of dust grains which are collisionally heated (neglecting the grain charge) in the filaments. For these temperatures and densities, 0.1 μm grains will have a temperature of ~ 23 K. Smaller grains are warmer however (e.g., ~ 34 K for 0.01 μm grains), and integration of the IR emission over a distribution of grain sizes can produce the appropriate 60–100 μm color temperature of 30 K. Assuming that the bulk of 12 and 25 μm emission is actually related to the optical filaments poses a problem, though. The smallest grains can achieve equilibrium temperatures of only ~ 60 K, too low to account for the 12 and 25 μm emission. Stochastically heated grains can, in principle, produce emission at these wavelengths; however, for such a high density and low tem-

perature, only grains smaller than ~ 50 Å undergo the stochastic heating. As a result, the 12 and 25 μm emission is extremely sensitive to the abundance of the very smallest grains. However, even though short-wavelength emission can be produced by very small grains, we were unable to find a continuous power-law distribution of grain sizes which could produce a spectrum matching the short-wavelength and long-wavelength emission simultaneously. In these models, a separate component of very small grains, or perhaps PAHs, is required to provide an adequate fit to the spectrum at all wavelengths. Future higher resolution observations will provide better measurements of the strength of 12 and 25 μm emission associated with the optical filaments, and thus a more accurate assessment of the small grain component.

As mentioned above, we applied collisional heating models neglecting the grain charge. This is permissible at temperatures above $\sim 10^6$ K (Draine 1981; McKee et al. 1987) where electrostatic potential energy, eU, is less than the kinetic energy of the gas particles, $\sim kT$, i.e., $|\phi| \equiv |eU/kT| \ll 1$. However, at temperatures of $\sim 10^4$ K, the grains are negatively charged, significantly reducing the electron collision cross section of the grain and thus the grain heating. The increased cross section for collisions with protons and positive ions does not make up for the lost energy deposition of electrons. While the dust is found to be cooler when grain charge is included, the qualitative results are similar to the case for uncharged grains but are now even more pronounced. Namely, the equilibrium temperatures of the large grains are much lower than the 60–100 μm color temperature; the 12 and 25 μm emission can be produced only by very small grains; and it is difficult to fit the observed spectrum without very careful tailoring of the grain size distribution.

Absorption of the ambient radiation can also be a significant heating source for the dust in the filaments. Calculating the intensity of the radiation heating the dust is somewhat uncertain due to the unknown and variable geometry of the dust and the filaments. The resolution of *IRAS* data does not allow us to determine whether the emitting dust is within or simply nearby the filaments. In the following analysis we will make assumptions which will tend to maximize the contribution of radiative heating. From the optical and UV spectra of one of the brightest filaments (see D'Odorico et al. 1980) we estimate that the amount of emission in optical and UV lines and the UV 2 photon continuum is ~ 70 times greater than the Hβ flux, and the total surface brightness in the UV and optical is $\sim 7 \times 10^{-3}$ ergs s^{-1} cm^{-2} sr^{-1}. The total IR emission associated with the IR filaments is roughly equal to the Hβ fluxes measured by FBK. Therefore the energy of optical filaments is clearly sufficient to account for the IR emission. Assuming that the dust is completely surrounded (4π sr) by filaments of the brightness quoted above, the optical and UV radiation is also strong enough to heat the dust to temperatures of ~ 30 K, as required to fit the 60–100 μm color temperature. However if the radiation is more or less intense by a factor of ~ 5, then the dust will be either too warm or too cool to match the observed emission. The UV emission provides stochastic heating for the smaller dust grains and enables the production of 12 and 25 μm emission, although the calculated 12 μm emission is always weaker than the observed emission for any power-law grain size distribution.

The effects of radiative and collisional heating acting simultaneously can yield a good fit to the data (Fig. 9), but there is still strong sensitivity to the abundance of small grains. A

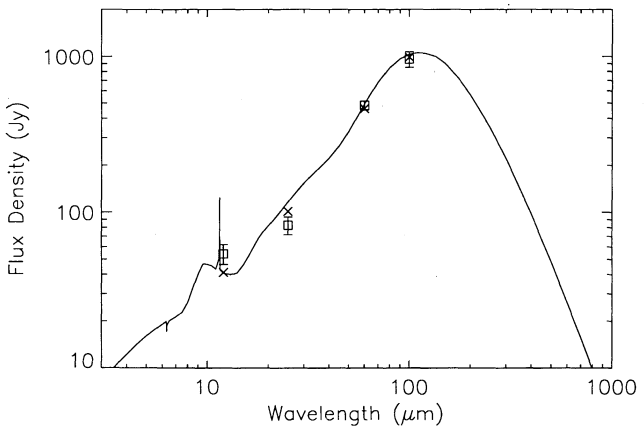

FIG. 9.—The total intensity spectrum of the IR component associated with the optical emission, and the best-fitting dust emission model including both radiative and collisional heating. The boxes with 1 σ error bars indicate the IR data. The line indicates the model spectrum. The crosses indicate the model spectrum integrated over the *IRAS* bands for comparison with the observed data points.

MRN distribution of grain sizes extended to minimum grain sizes of 3 Å and with a change of the power law index from -3.5 to -4.5 between 3 and 10 Å for both graphite and silicate grains is needed to produce the best fit. A similar enhancement in the population of very small grains was required to fit the IR spectra of high-latitude cirrus clouds (Draine & Anderson 1985; Weiland et al. 1986). Collisional heating appears to be more effective for the small stochastically heated grains ($a < 100$ Å), while radiative heating dominates for the larger grains which reside at their equilibrium temperatures. Whether radiative and collisional heating act separately or together, thermal emission from dust cannot account for all of the 12 μm emission of the optical filaments, and can only account for the 25 μm emission if small grains ($a \lesssim 100$ Å) are present. This suggests that lines may be contributing to the IR emission of the filaments.

5.2. *Infrared Line Emission*

Finally, we consider line emission which may also contribute to the observed IR fluxes associated with the filaments. Raymond (1979) and Shull & McKee (1979) have computed the optical and IR line intensities for a series of shock models. Several of the models produce good matches to the optical emission at some locations in the Cygnus Loop (see FBK). We have measured the optically associated IR emission at several locations around the remnant which were studied by FBK. The shock models were used to derive the expected intensity of IR lines from the optical data of FBK. The measured IR emission at several locations is compared with the predicted line emission in Figure 10. The measured fluxes are very uncertain due to large difference in resolution between the optical and IR data. The derived intensities of the IR line emission are also uncertain because different models can be chosen to represent the region of interest, and because the Raymond (1979) and the Shull & McKee (1979) models do not include the same lines (and perhaps not all of the important lines) in each of the *IRAS* bands. Despite this, they suggest that typically between $\sim 10\%$ and 100% of the emission in the *IRAS* bands is due to lines. The fraction varies with region, model, and *IRAS* band considered, but it illustrates that theoretical models predict that IR lines contribute a significant fraction of the IR emission associ-

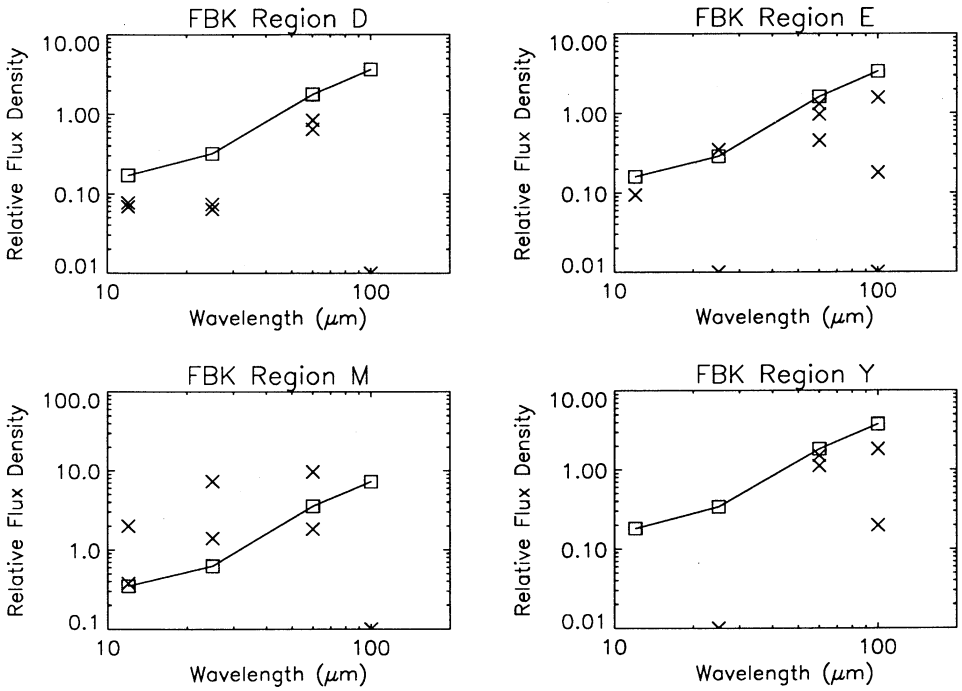

FIG. 10.—Comparison of the IR emission associated with several optical filaments (*open squares*) with the amount of line emission predicted by Raymond (1979) and Shull & McKee (1979) models (*crosses*) which provide reasonable fits of the optical spectra (Fesen, Blair, & Kirshner 1982). Generally ~10% to ≳100% of the observed emission may be atributed to lines. Raymond (1979) models do not include any lines in the 100 μm band, while Shull & McKee (1979) models do not include any lines in the 25 μm band, and only include one weak line in the 12 μm band.

ated with the optical filaments. If this is indeed the case, then the IR spectrum of the filaments cannot yield any information on associated dust, unless a reliable means of prediction (or observing) the line emission in the *IRAS* bands is found.

6. IMPLICATIONS

6.1. *Comparison with Previous Studies*

Previous measurements of the emission of the Cygnus Loop in the *IRAS* bands have been reported by Braun & Strom (1986b), Dwek et al. (1987b), Arendt (1989), and Saken, Fesen, & Shull (1992). The flux densities reported here are higher (and more accurate) than the very uncertain flux densities reported by Arendt (1989). Dwek et al. (1987b) reported a total IR flux of 7.9×10^{-8} ergs s^{-1} cm^{-2} which is about half of the 1.8×10^{-7} ergs s^{-1} cm^{-2} which we find in this present study, and believe to be more accurate. Comparing the fraction of the IR flux associated with the X-ray shell with the observed X-ray flux (Ku et al. 1984) yields an IRX ratio of 7.9. Including a correction factor for nonequilibrium ionization effects (see Dwek et al. 1987b) gives a final IRX ratio of ~11. This closer to agreement with the theoretically expected ratio than the value of Dwek et al. (1987b). The remaining difference may be due to the value of a_{min}, used for calculating the expected IRX ratio (Dwek et al. 1987b), which is smaller than the grains we find in the Cygnus Loop. A new survey of SNRs in the IR by Saken et al. (1992) finds flux densities for the Cygnus Loop in good agreement with those found here.

Another previous study of the IR emission of the Cygnus Loop was completed by Braun & Strom (1986b) using a different approach than the one used here. They first separated the remnant from the background emission by decomposing the IR emission into a warm component associated with the SNR and a spatially uncorrelated, cool component attributed to background clouds. This method is most effective when the spectrum of the SNR is uniform across the remnant and distinctly different from that of the confusing emission. Braun & Strom (1986b) find noticeably higher and lower flux densities at 25 and 100 μm respectively. This is probably due to different effective background levels used.

To separate a source from the confusing background in the IR data, one needs to be able to recognize the source by either a distinguishing spectrum or morphology (or both). Thus, a known spectrum of an extended source can aid in determining the morphology of the source, or if the extent of an source is well known, the source spectrum can be extracted. The spectral separation technique used by Braun & Strom (1986b) can allow the identification of source features which lack corresponding emission outside of the IR regime, e.g., the small extension to the NW of the shell which they find. Our morphological separation of emission can identify emission associated with a SNR even if it is spectrally indistinguishable from the background emission.

Once they isolated the emission of the remnant, Braun & Strom divided the IR emission into a shock-heated component, which is apparently associated with both the fast X-ray–producing shocks and the shower optical shocks, and a "recombined" component, which is assumed to be depleted of small dust grains and reside in very cool recombined gas within the remnant where it is only heated by the interstellar radiation field (ISRF). This separation is done by assuming that the spectrum of the recombined component is the same as that of the cool background features at 60 and 100 μm and zero at 12 and 25 μm. The spectrum of the shock-heated dust

then becomes that characteristic of dust uniformly radiating at $T_{dust} \approx 60$ K. This process and its results are inconsistent with the results found here and with theoretical expectations. We find a color temperature of only $T_{dust} = 31$ K for the X-ray shell. At the relatively low temperatures (~ 1–4×10^6 K) in the X-ray shell of the Cygnus Loop, the 60 K dust temperature found by Braun & Strom would require densities $\gtrsim 100$ cm^{-3} which are not supported by X-ray observations. Furthermore, the shock-heated gas (whether associated with optical or X-ray emission) should contain dust emitting over a range of temperatures rather than the single temperature implied by the spectrum found by Braun & Strom (1986b), unless the gas is hotter than $\sim 10^7$ K and stochastic effects are unimportant (Dwek 1986, 1987). Neither of these exemptions apply for the Cygnus Loop. The success of our decomposition of the IR emission into components associated with the X-ray and optical emission leaves no room for a component associated with recombined gas, unless this neutral gas has the same distribution as the X-ray or optical emission.

6.2. *Comparison to Other Remnants: Environmental Influences*

A comparison of the Cygnus Loop with other middle-aged SNRs shows how the ambient environment controls the observed emission of these objects.

Puppis A (Arendt et al. 1990, 1991) shows no global relation between its IR and optical emission, but does show excellent correlation between its IR and X-ray emission. The IR emission of Puppis A is consistent with thermal emission from collisionally heated dust grains. Puppis A is sweeping up dust from a nearby cloud, and sputtering of this dust takes place on a time scale comparable to the age of the SNR (Arendt et al. 1991). The ISM in the vicinity of Puppis A is not grossly different from that near the Cygnus Loop. The differences between the remnants in their morphological relations between IR and optical emission primarily reflect the age difference of the two SNRs. Puppis A is only a fraction of the age of the Cygnus Loop and does not possess an extensive system of slower, optically emitting shocks.

IC 443 (Braun & Strom 1986a; Mufson et al. 1986) has an age which is more comparable to that of the Cygnus Loop. In the northeast portion of the remnant there is well developed optical emission which, like that of the Cygnus Loop, is well correlated with IR emission. Unlike the Cygnus Loop however, IC 443 shows no relation between IR and X-ray emission. There is strong correspondence between shock-excited H_2 and [O I] emission and IR in the southern half of the remnant (Burton et al. 1988, 1990) where IC 443 is expanding into a dense molecular cloud. Much weaker shock-excited H_2 emission has been observed ahead of the optically visible shocks in the northeast portion of the Cygnus Loop (Graham et al. 1991), but this emission is not related to any dense molecular cloud being swept up by the remnant. Thus the differences between the Cygnus Loop and IC 443 are due more to different environments than different ages.

These comparisons show that for the purposes of analyzing the IR morphology of SNRs we can broadly categorize the ISM into four density regimes.

1. High-density regions (i.e., dense molecular clouds) show relatively weak optical and radio emission, little or no X-ray emission, and strong IR emission which correlates with shocked H_2 emission. An example of such a region is the southern portion of IC 443.

2. Regions of moderate density (such as H I clouds) have faster shocks characterized by strong optical and radio filaments. IR emission is found associated with the filaments, but its nature and whether it is correlated in detail is unknown. X-ray emission often envelops, or lies immediately behind, the filaments. Examples of these regions are the East Knot of Puppis A, the northeast optical/radio filaments (and perhaps the southwest also) of IC 443, and the bright optical filaments in the Cygnus Loop.

3. Low-density intercloud regions are where the SNR shocks propagate fastest and give rise to the most distinct X-ray emission. If optical emission is seen, it is faint and dominated by Balmer emission. IR emission is thermal emission from collisionally heated dust grains and is very well correlated with the X-ray emission in these regions. Radio emission is generally weaker than in denser regions. Examples of these regions are: most of Puppis A, and the X-ray shell of the Cygnus Loop. In somewhat younger remnants like Puppis A, the higher speed of the shocks may tend to give rise to these same emission characteristics in regions of moderate density.

4. Regions of very low density, which presumably give rise to the breakouts seen in some SNRs, are harder to characterize. Judging from the Cygnus Loop and the probable breakout in IC 443, a breakout is outlined by optical filaments near the confined portion of the SNR. It can also show radio limb brightening, and perhaps diffuse radio emission from the interior. X-ray emission is faint. IR emission may be correlated with the optical emission, but is relatively weak. These properties apply to the south portion of the Cygnus Loop and the filament extending northeast from IC 443.

An immediate result that can be inferred from this classification scheme is that we can conclude that the Cygnus Loop is not interacting with any dense molecular clouds, since all of its IR emission is associated with either optical emission (indicating moderate-density H I clouds) or X-ray emission (indicating low-density intercloud material). Indeed, to date there are no studies indicating a strong interaction between the Cygnus Loop and surrounding molecular clouds. A molecular cloud observed to the west of the western optical filaments (Scoville et al. 1977) does not show accelerated material or strong IR emission as does the cloud which is being hit by IC 443 (Braun & Strom 1986a; Mufson et al. 1986; and references therein).

The age of a SNR also plays an important role in determining the dominant emission and the correlations between various wavelengths. Young remnants with significantly higher shock speeds, such as Tycho, Kepler, and Cas A, do not show correlations which can be easily fit into the scheme above. Likewise, very old SNRs such as CTB 80 (Fesen, Shull, & Saken 1988) and OA 184 (Leahy & Marshall 1988) exhibit different emission correlations as a function of density. In these old, slowly expanding SNRs the heating of the dust by the ISRF plays a more important role than in younger SNRs.

7. SUMMARY

The IR emission of the Cygnus Loop is well correlated with the X-ray and optical emission of the remnant. These correlations imply that the IR emission arises from two distinct regions of the remnant: the X-ray shell, and the optical filaments. The fact that the X-ray and optical morphologies do not correlate in all regions of the remnant allows us to decompose the IR emission into two distinct components:

1. *The IR emission from the X-ray shell.*—This emission is from collisionally heated dust with a temperature of ~ 31 K.

Detailed modeling of the IR emission, which includes the stochastic heating effects in small grains, suggests a deficiency of grains with radii below ~ 150 Å in the shocked gas, compared to grain size distribution found in the general ISM. The deficiency of small grains is difficult to explain by thermal sputtering within the lifetime of the SNR.

2. *The IR emission from the optical filaments.*—Assuming that all of this emission is thermal emission from dust, we derive a dust temperature of ~ 30 K. This dust could be either collisionally or radiatively heated within the filaments. Shock models show that a significant fraction of the IR flux may be due to fine-structure lines. The relative contribution of line emission in the various *IRAS* bands is presently unclear.

The IR analysis allows us to determine the following remnant parameters: In the X-ray shell, we find a gas mass of $\sim 70\ M_\odot$ from the dust mass of $\sim 0.5\ M_\odot$ and an assumed undepleted dust to gas mass ratio of 0.0075. From the angular radius of the shell and the distance, we calculate the volume and determine that the mean density of the unshocked ISM is $\sim 0.07\ \mathrm{cm}^{-3}$. The gas temperature required to heat the dust to 31 K is $\sim 3 \times 10^6$ K, in agreement with X-ray determinations. Assuming the shell to be in the Sedov phase, we estimate the age of the remnant to be $\sim 15{,}000$ yr and an initial explosion energy of $\sim 0.26 \times 10^{51}$ ergs.

The IR morphology of the Cygnus Loop bears some resemblance to those of Puppis A and IC 443 in terms of complexity, strength, and correlation with emission at other wavelengths. The similarities and differences between these remnants give some indication of how the structure of the external medium influences the IR emission of a SNR.

We wish to thank the referee whose constructive criticism has helped to make this a better paper. We thank Theodore R. Gull for providing the optical image of the Cygnus Loop, and Daniel A. Klinglesmith III for digitizing the photographic plate. R. Arendt acknowledges the support of the National Research Council Associateship program during the completion of this work. E. Dwek acknowledges support under NASA RTOP 188-44-53-05.

REFERENCES

Arendt, R. G. 1989, ApJS, 70, 181
Arendt, R. G., Dwek, E., & Petre, R. 1991, ApJ, 368, 474
Arendt, R. G., Dwek, E., Petre, R., Dickel, J. R., Roger, R. S., Milne, D. K., & Kesteven, M. J. 1990, ApJ, 350, 266
Ballet, J., & Rothenflug, R. 1989, A&A, 218, 277
Blair, W. P., Long, K. S., Vancura, O., & Holberg, J. B. 1991, ApJ, 374, 202
Braun, R., & Strom, R. G. 1986a, A&A, 164, 193
———. 1986b, A&A, 164, 208
Burton, M. G., Geballe, T. R., Brand, P. W. J. L., & Webster, A. S. 1988, MNRAS, 231, 617
Burton, M. G., Hollenbach, D. J., Haas, M. R., & Erickson, E. F. 1990, ApJ, 355, 197
Charles, P. A., Kahn, S. M., & McKee, C. F. 1985, ApJ, 295, 456 (CKM)
D'Odorico, S., Benvenuti, P., Dennefeld, M., Dopita, M. A., & Greve, A. 1980, A&A, 92, 22
DeNoyer, L. K. 1975, ApJ, 196, 479
Draine, B. T. 1981, ApJ, 245, 880
Draine, B. T., & Anderson, N. 1985, ApJ, 292, 494
Draine, B. T., & Lee, H. M. 1984, ApJ, 258, 89
Draine, B. T., & Salpeter, E. E. 1979, ApJ, 231, 77
Dwek, E. 1981, ApJ, 247, 614
———. 1986, ApJ, 302, 363
———. 1987, ApJ, 322, 812
———. 1988, in Supernova Remnants and the Interstellar Medium, ed. R. S. Roger & T. L. Landecker (Cambridge: Cambridge Univ. Press), 363
Dwek, E., & Arendt, R. G. 1992, ARA&A, in press
Dwek, E., Dinerstein, H. L., Gillett, F. C., Hauser, M. G., & Rice, W. L. 1987a, ApJ, 315, 571
Dwek, E., Petre, R., Szymkowiak, A., & Rice, W. L. 1987b, ApJ, 320, L27
Fesen, R. A., Blair, W. P., & Kirshner, R. P. 1982, ApJ, 262, 171 (FBK)
Fesen, R. A., Shull, J. M., & Saken, J. M. 1988, Nature, 334, 229
Graham, J. R., Wright, G. S., Hester, J. J., & Longmore, A. J. 1991, AJ, 101, 175
Green, D. A. 1990, AJ, 100, 1927
Hatsukade, I., & Tsunemi, H. 1990, ApJ, 362, 566
Hauser, M. G., et al. 1984, ApJ, 278, L15
Hauser, M. G., & Vrtilek, J. 1992, in preparation
Hester, J. J., & Cox, D. P. 1986, ApJ, 300, 675
Hester, J. J., Raymond, J. C., & Danielson, G. E. 1986, ApJ, 303, L17
Hubble, E. P. 1937, Carnegie Yrb., 36, 189
Keen, N. J., Wilson, W. E., Halsam, C. G. T., Graham, D. A., & Thomasson, P. 1973, A&A, 28, 197
Ku, W. H.-M., Kahn, S. M., Pisarski, R., & Long, K. 1984, ApJ, 278, 615
Leahy, D. A., & Marshall, C. R. 1988, MNRAS, 235, 805
Mathis, J. S., Rumpl, W., & Nordsieck, K. H. 1977, ApJ, 217, 425
McKee, C. F., Hollenbach, D. J., Seab, C. G., & Tielens, A. G. G. M. 1987, ApJ, 318, 674
Miller, J. S. 1974, ApJ, 189, 239
Minkowski, R. 1958, Rev. Mod. Phys., 30, 1048
Mufson, S. L., McCullough, M. L., Dickel, J. R., Petre, R., White, R., & Chevalier, R. 1986, AJ, 92, 1349
Raymond, J. C. 1979, ApJS, 39, 1
Raymond, J. C., Black, J. H., Dupree, A. K., Hartmann, L., & Wolff, R. S. 1980a, ApJ, 238, 881
Raymond, J. C., Blair, W. P., Fesen, R. A., & Gull, T. R. 1983, ApJ, 275, 636
Raymond, J. C., Cox, D. P., & Smith, B. W. 1976, ApJ, 204, 290
Raymond, J. C., Davis, M., Gull, T. R., & Parker, R. A. R. 1980b, ApJ, 238, L21
Saken, J. M., Fesen, R. A., & Shull, J. M. 1992, ApJS, 81, 715
Scoville, N. Z., Irvine, W. M., Wannier, P. G., & Predmore, C. R. 1977, ApJ, 216, 320
Seab, C. G. 1987, in Interstellar Processes, ed. D. J. Hollenbach & H. A. Thronson, Jr. (Dordrecht: Reidel), 491
Seward, F. D. 1990, ApJS, 73, 781
Shull, J. M., & McKee, C. F. 1979, ApJ, 227, 131
Tsunemi, H., Manabe, M., Yamashita, K., & Koyama, K. 1988, PASJ, 40, 449
Vedder, P. W., Canizares, C. R., Markert, T. H., & Pradhan, A. K. 1986, ApJ, 307, 269
Weiland, J. L., Blitz, L., Dwek, E., Hauser, M. G., Magnini, L., & Rickard, L. J. 1986, ApJ, 306, L101